Supporting Information

Methanol upgrading coupled with hydrogen product at large current density promoted by strong interfacial interaction

Yixin Hao, Deshuang Yu, Shangqian Zhu, Chun-Han Kuo, Yu-Ming Chang, Luqi Wang, Han-Yi Chen, Minhua Shao, and Shengjie Peng*

Y. Hao, D. Yu, L. Wang, Prof. L. Li, Prof. S. Peng
Jiangsu Key Laboratory of Electrochemical Energy Storage Technologies
College of Materials Science and Technology
Nanjing University of Aeronautics and Astronautics
Nanjing 210016, China
E-mail: pengshengjie@nuaa.edu.cn
Dr. S. Zhu, Prof. M. Shao
Department of Chemical and Biological Engineering
The Hong Kong University of Science and Technology, Kowloon, Hong Kong, China
Y. Chang, C. Kuo, Prof. H. Chen
Department of Materials Science and Engineering
National Tsing Hua University, Hsinchu 30013, Taiwan
Prof. M. Shao
Energy Institute
The Hong Kong University of Science and Technology, Kowloon, Hong Kong, China

1 Method

1.1 Chemicals

Nickel foam, Ferric (II) chloride ($FeCl_3$), and RuO_2 (99.9% trace metals basis) were purchased from Macklin. KOH (GR), methanol (GR), ethanol (AR), toluene (AR), and isopropanol (AR) were purchased from Sigma-Aldrich (Shanghai, China). All of the above chemicals were analytical grade and used as received without further purification.

1.2 Synthesis

Fe-NF-X catalysts were prepared through a one-step combustion method. First, different concentrations of $FeCl_3$ (0 mM, 100 mM, 200 mM, 300 mM, 400 mM, 500 mM, 600 mM, and 700 mM) were dissolved in ethanol to prepare salt solutions. Several pieces of nickel foam were immersed into the above solutions and then ignited at room temperature. After natural cooling, the products were labeled as Fe-NF-0, Fe-NF-100, Fe-NF-200, Fe-NF-300, Fe-NF-400, Fe-NF-500, Fe-NF-600, and Fe-NF-700, respectively. During the synthesis process, the Ni foam was served as not only the substrate but also as the Ni source.

1.3 Preparation of working electrode

To prepare RuO_2 electrode for comparison, the commercial active catalyst, carbon black (super P), and PVDF (polyvinylidene difluoride) were placed in a mortar with the mass ratio of 7:2:1, and NMP (N-methylpyrrolidone) was used as the solvent. Next, the mashed slurry was evenly coated on the Ni foam with an effective area of 1 cm^2.

The $MoNi_4/MoO_2$ electrocatalyst for HER was constructed on nickel foam through hydrothermal reaction and heat treatment [1]. First, the commercial nickel foam was successively washed with ethanol, 1 M HCl aqueous solution, and deionized water. Second, one piece of nickel foam was immersed into 15 mL of H_2O containing $Ni(NO_3)_2 \cdot 6H_2O$ (0.04 M) and $(NH_4)_6Mo_7O_{24} \cdot 4H_2O$ (0.01 M) in a Teflon autoclave. Third, the autoclave was heated at 150 ˚C for 6 h in a drying oven. After washing with deionized water, the $NiMoO_4$ cuboids were achieved on the nickel foam. Finally, the as-constructed $NiMoO_4$ cuboids were heated at 500 ˚C for 2 h in an H_2/Ar atmosphere, and then, the $MoNi_4$ electrocatalyst anchored on the MoO_2 cuboids was obtained.

1.4 Electrocatalytic experiments

The electrochemical characterizations were conducted in a three-electrode system with carbon electrode and Ag/AgCl (saturated KCl) electrode used as the counter electrode and reference electrode, respectively. The measurements were carried out on an Autolab electrochemical workstation (Autolab Instrument) at room temperature. To investigate the MOR activity, the prepared nickel foam-based binder-free electrode was cut into a size of 1.0

cm × 1.0 cm and used as a working electrode, and the electrochemical test was carried out in N_2 saturated 1.0 M KOH with or without 1.0 M methanol. The measured potentials versus Ag/AgCl were converted to the reversible hydrogen electrode (vs. RHE) according to the following equation: $E_{\text{vs RHE}} = E_{\text{vs Ag/AgCl}} + E_{\text{RHE vs Ag/AgCl}}$. The potentials were corrected through a manual post-correction approach according to the formula: $E=E_{\text{applied}} - iR$, where i is the current flowing through the cell, and R is the ohmic resistance of the cell.

Electrochemical impedance spectroscopy (EIS) measurements were carried out in the frequency range of 0.01-100 kHz at 1.35 V (vs. RHE) with AC amplitude of 5 mV. The double-layer capacitance (C_{dl}) was obtained by collecting CV curves with scan rates of 20 to 100 mV s^{-1}. The linear sweep voltammograms (LSV) and cyclic voltammetry (CV) curves were carried out at a scan rate of 5 mV s^{-1} and 50 mV s^{-1} respectively. The LSV and CV of the catalysts for MOR and OER were measured in a range of 1.18 - 1.98 V vs. RHE.

A Nicolet iS50 FTIR spectrometer equipped with a mercury cadmium telluride detector cooled with liquid nitrogen was employed for the in situ FTIR studies. Catalysts were dispersed on a glassy carbon electrode and pressed against a CaF_2 prism. An Ag/AgCl and Pt wire were used as the reference and counter electrodes, respectively. All spectra are shown in absorbance [-log(R/R_0)], with R and R_0 representing the sample and reference spectra, respectively. Real-time IR spectra were continuously collected during linearly sweeping the potential of working electrode from 1.0 to 2.1 V vs RHE at a scanning rate of 5 mV s^{-1}. The spectral resolution is 8 cm^{-1} with 44 scans per spectrum (a collection duration of 10 s). IR background was taken at 1.0 V vs RHE. Spectra under s- and p-polarized IR beams were collected by the same methodology.

1.5 Characterization

The morphologies of catalysts were observed by SEM (JEOL JSM-7600F) and HR-TEM (TEM; JEOL JEM-2100F). The elemental compositions were analyzed by EDS attached to the TEM. The XRD patterns of the catalysts were collected by X-ray diffraction (Shimadzu XRD-6000, Cu KR radiation, λ = 1.5418 Å). XPS analysis was recorded on Kratos Axis Ultra DLD electron spectrometer at an accelerating voltage of 13 kV and a pass energy of 35.75 eV (PHI, PHI5300 system). The content of metal elements was determined by inductively coupled plasma emission spectroscopy (ICP, LEEMON, PRODIGY XP). The extended X-ray absorption fine structure (EXAFS) was measured at Taiwan Photon Source (TPS) beamline, 44A Quick-scanning X-ray absorption spectroscopy (XAS), in National Synchrotron Radiation Research Center (NSRRC), Hsinchu, Taiwan.

The identification of the molecular structure of formate in the anode product is conducted by Nuclear magnetic resonance (NMR) spectroscopy recorded by Bruker AVANCE III

600MHz instruments (^{13}C NMR). The identification and quantification of formate products are conducted by Ion Chromatography (IC) and determined by calibration curve. The anode solution was then proportionately diluted and analyzed by Ion Chromatography (IC) to detect the formate generation.

1.6 product quantification

The Faradaic efficiency (FE) of formate generation was calculated using the following equation:

$$\mathrm{FE(formate,\%)} = \frac{\text{mole of formed formate}}{\text{total charge passed} / (4 \times F)} \times 100\%$$

$$\mathrm{FE(formate,\%)} = \frac{4 \times 96485(\frac{\mathrm{C}}{mol}) \times \omega_t(\frac{mg}{\mathrm{L}}) \times \mathrm{V(L)} \times 10^{-3}(\frac{\mathrm{g}}{mg})}{M_{formate}(\frac{\mathrm{g}}{mol}) \times \int_0^t I(A)dt} \times 100\%$$

where F is the Faraday constant (96485 C mol^{-1}). ω_t(mg L^{-1}) is the concentration of formed formate in the solution from the anode compartment of the cell, namely, the IC data (ppm × 10^{-6}). The unit of ppm here is mass(formate)/volume(solution). V(L) is the total volume of the solution in the anode compartment of the cell. $M_{formate}$(g mol^{-1}) is the molecular weight of formate (HCOO$^-$) equal to 45.02 g mol^{-1}.

The generated H_2 at the cathode and the possible gaseous product (e.g. O_2) at the anode were determined by gas chromatography with a thermal conductivity detector (TCD).

The Faradaic efficiency (FE) of H_2 production was calculated using the following equation:

$$\mathrm{FE(H_2,\%)} = \frac{\text{mole of formed } \mathrm{H_2}}{\text{total charge passed} / (2 \times F)} \times 100\%$$

$$\mathrm{FE(H_2,\%)} = \frac{2\mathrm{FV}vp_0}{\mathrm{RT_0}I} \times 100\%$$

$$\mathrm{FE(H_2,\%)} = \frac{2 \times 96485(\frac{\mathrm{C}}{mol}) \times \mathrm{V}(\frac{m^3}{s}) \times v(vol\ ratio) \times 1.01 \times 10^5(\frac{\mathrm{N}}{m^2})}{8.314(\frac{\mathrm{N}\,m}{mol\,\mathrm{K}}) \times 298.15(\mathrm{K}) \times I(\mathrm{A})} \times 100\%$$

where F is the Faraday constant (96485 C mol^{-1}). v(vol ratio) is the volume concentration of H_2 in the exhaust gas from the cathode compartment of the cell, namely, the GC data (volume ppm × 10^{-6}). The unit of ppm here is volume(H_2)/volume(total). V(m^3 s^{-1}) is the gas flow rate measured by a flow meter at room temperature and under ambient pressure. I(A) is the current recorded by the electrochemical workstation in the chronoamperometry (*I-t*) mode.

1.7 Computational details

All DFT calculations were performed using the Vienna Ab initio Simulation Package (VASP)[1]. The projector augmented wave (PAW)[2] pseudopotential with the PBE[3] generalized gradient approximation (GGA) exchange correlation function was utilized in the computations. All energetics of metal oxides were calculated using the DFT with the Hubbard-U framework (DFT + U) to account for strongly localized d-electrons for Fe, and Ni. The Hubbard-U correction terms were at U_{eff}(Ni) = 6.2 eV and U_{eff}(Fe) = 5.3 eV as obtained via linear response theory. The cutoff energy of the plane waves basis set was 500 eV and a Monkhorst-Pack mesh of 2 × 2 × 1 was used in K-sampling. All structures were spin polarized and all atoms were fully relaxed with the energy convergence tolerance of 10^{-5} eV per atom, and the final force on each atom was < 0.05 eV $Å^{-1}$.

The adsorption energy of reaction intermediates can be computed using the following Equation:

$$\Delta G_{ads} = E_{ads} - E_{*} + \Delta E_{ZPE} - T\Delta S$$

Where ads = (CH_3OH*, CH_3O*, CH_2O*, CHO*, HCOOH*, HCOO*, CO_2*), and ($E_{ads} - E_{*}$) is the binding energy, ΔE_{ZPE} is the zero-point energy change, ΔS is the entropy change. In this work, the values of ΔE_{ZPE} and ΔS were obtained by vibration frequency calculation.

The Gibbs free energy of the five reaction steps can be calculated by the following four Equations:

$CH_3OH + * \text{——} *CH_3OH$

$*CH_3OH + OH^- \text{——} *CH_3O + H_2O + e^-$

$*CH_3O + OH^- \text{——} *CH_2O + H_2O + e^-$

$*CH_2O + OH^- \text{——} *CHO + H_2O + e^-$

$*CHO + OH^- \text{——} *HCOOH + e^-$

$*HCOOH + OH^- \text{——} *HCOO + H_2O + e^-$

$*HCOO + OH^- \text{——} *CO_2 + H_2O + e^-$

$*CO_2 \text{——} * + CO_2$

In this work, the Gibbs free energy was calculated at U = 0.

[1] J. Zhang, T. Wang, Z. Liao, X. Zhuang, M. Chen, E. Zschech, X. Feng, *Nat. Commun.* **2017**, 8,15437.

[2] G. Kresse, J.Furthmüller, *Phys. Rev. B* **1996**, *54*, 11169.

[3] P. E. Blöchl, *Phys. Rev. B* **1994**, *50*, 17953.

[4] J. P. Perdew, K. Burke, M. Ernzerhof, *Phys. Rev. Lett.* **1996**, 77, 3865.

2 Figures and tables

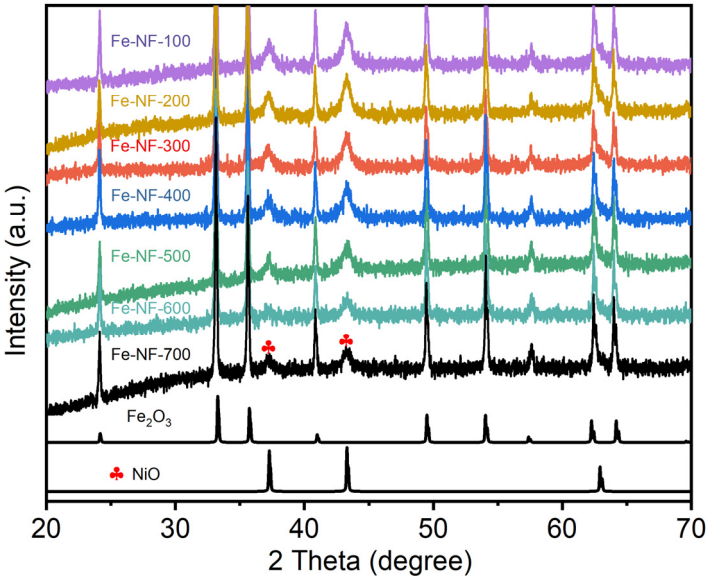

Figure S1. X-ray diffraction pattern of Fe-NF-100, Fe-NF-200, Fe-NF-300, Fe-NF-400, Fe-NF-500, Fe-NF-600 and Fe-NF-700, respectively.

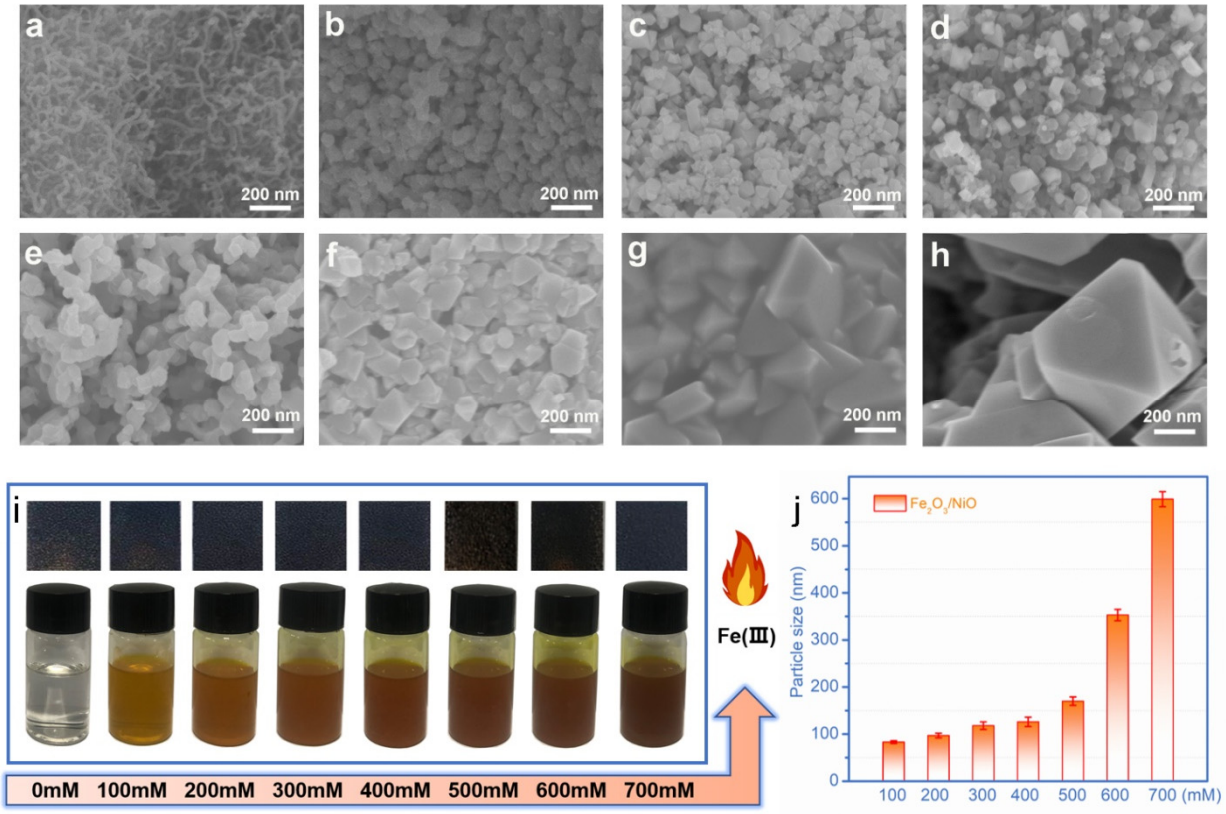

Figure S2. Preparation process and morphology information of extended experiments. FESEM images of (a) Fe-NF-0, (b) Fe-NF-100, (c) Fe-NF-200, (d) Fe-NF-300, (e) Fe-NF-400, (f) Fe-NF-500, (g) Fe-NF-600, (h) Fe-NF-700, (i) Photographs of Ni foam immersed in solutions with different concentrations, as well as photographs of post-combustion product. (j) The particles size distribution of the Fe_2O_3/NiO NPs.

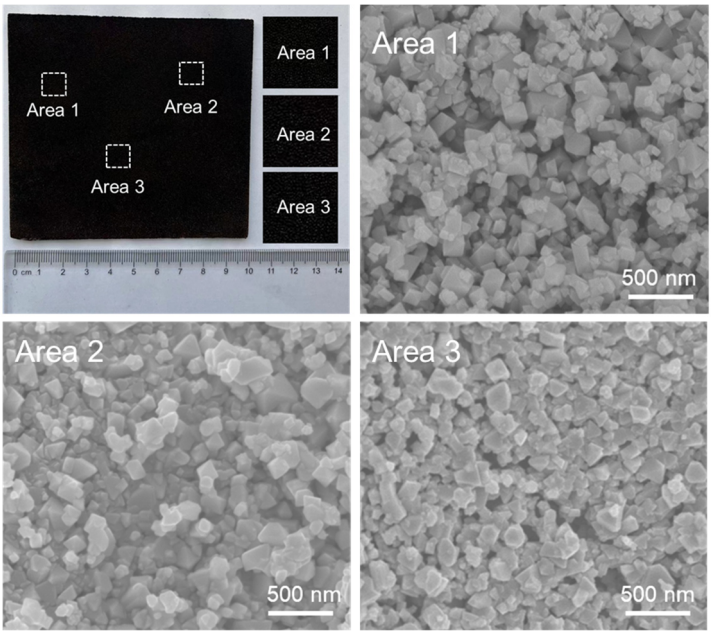

Figure. S3 Electronic photograph of a large-scale sample preparation and SEM images of different areas.

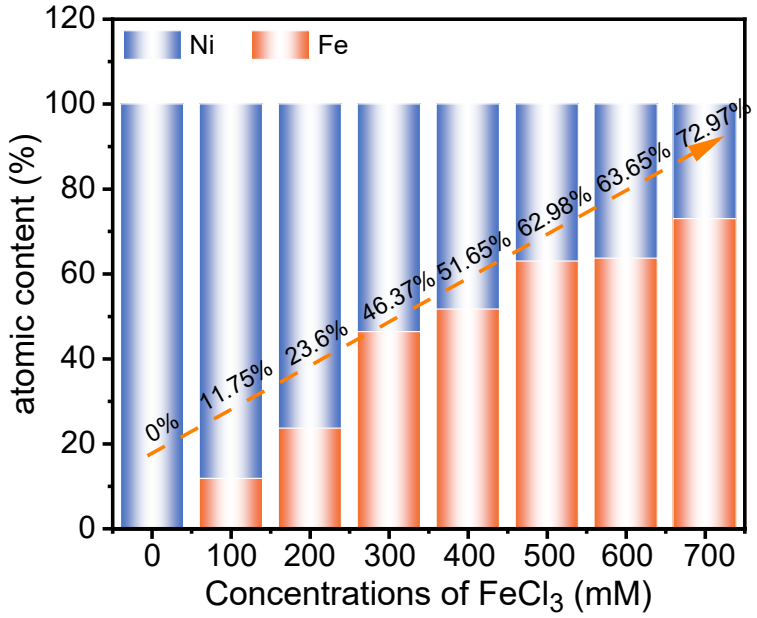

Figure S4. The molar ratio of Ni and Fe in the Fe -NF-X heterojunctions obtained by ICP.

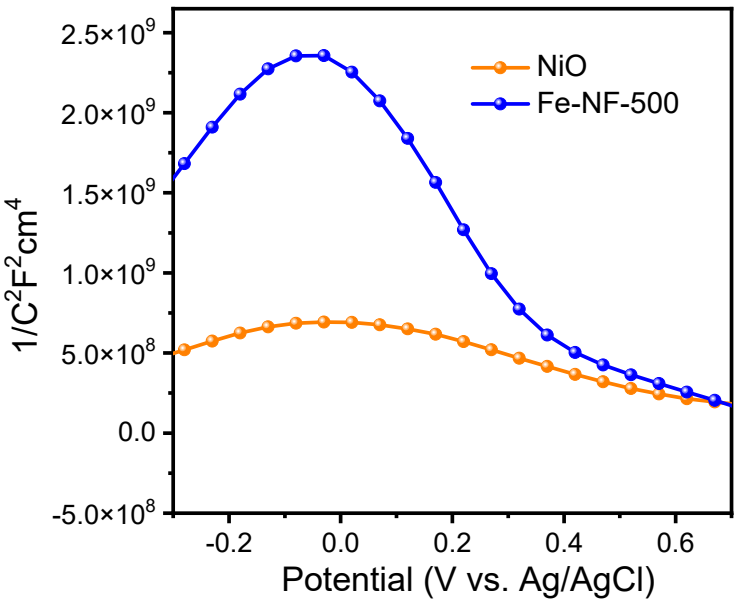

Figure S5. Mott-Schottky plots of NiO and Fe-NF-500.

It is generally believed that the heterojunction interface can create a potential barrier and prevent the flow of carriers across the junction interface. Therefore, the carrier concentration is negatively correlated with the interface concentration. The carrier concentration was collected by measuring Mott Schottky curves on an electrochemical workstation. Fe-NF-500 exhibits the highest slope representing the lowest carrier concentration, demonstrating the abundance of heterogeneous.

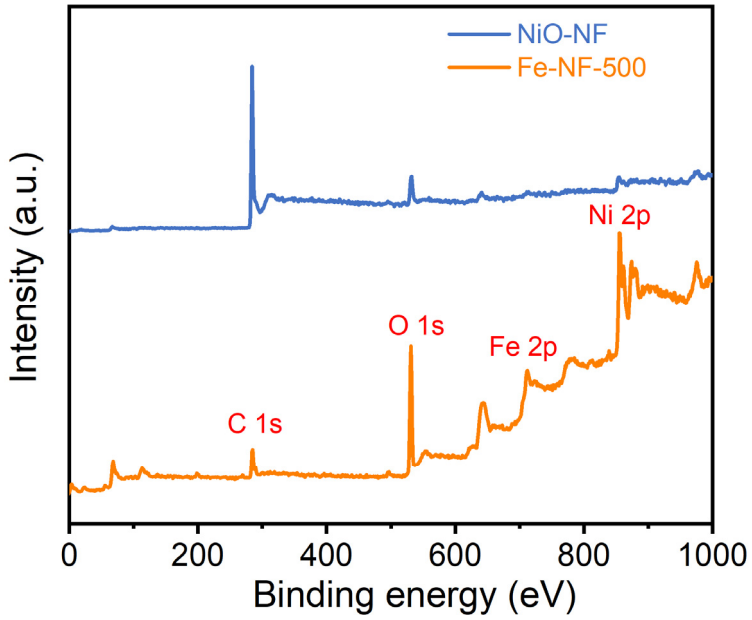

Figure S6. Survey XPS spectra of NiO-NF and Fe -NF-500.

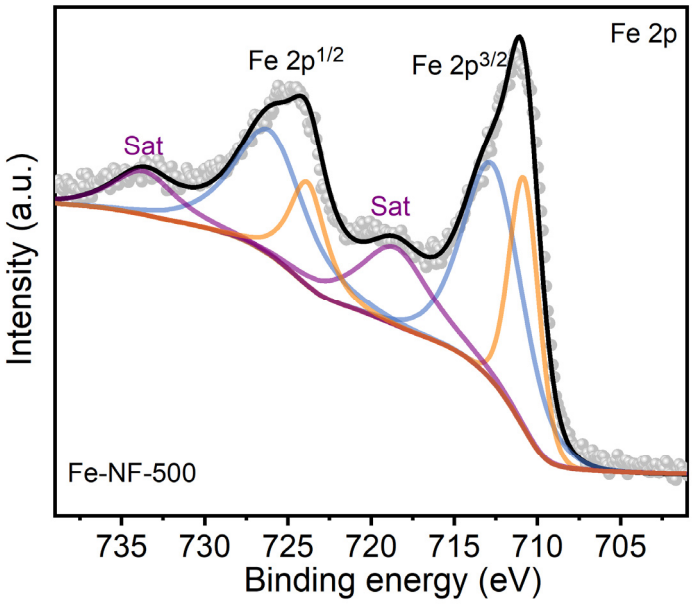

Figure S7. XPS spectra of Fe 2p in Fe-NF-500.

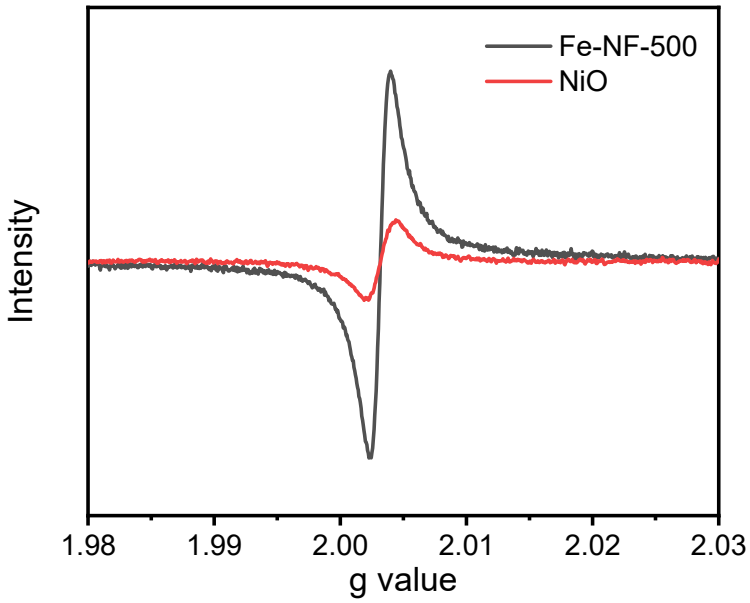

Figure S8. EPR spectra of Fe-NF-500 and as-prepared NiO, respectively.

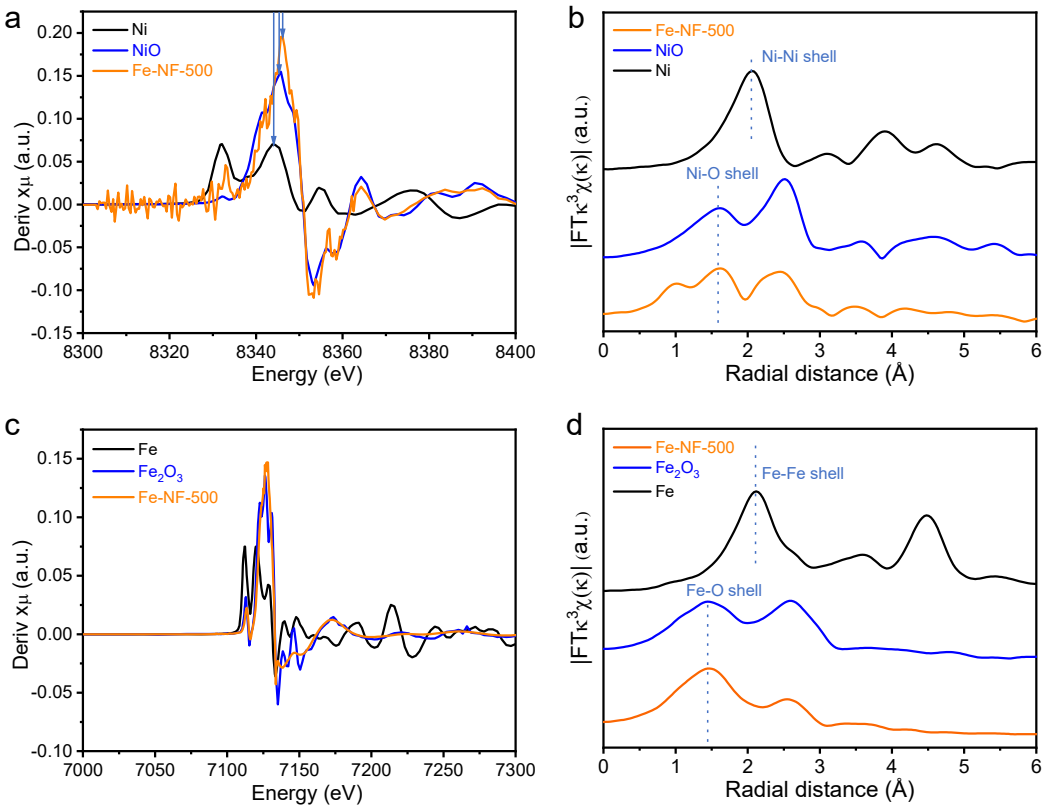

Figure S9. XAS characterization of catalysts. (a) first derivative spectra, and (b) FT-EXAFS spectra of Ni in Fe-NF-500, NiO, as well as Ni foil. (c) first derivative spectra, and (d) FT-EXAFS spectra of Fe in Fe-NF-500, Fe_2O_3, as well as Fe foil.

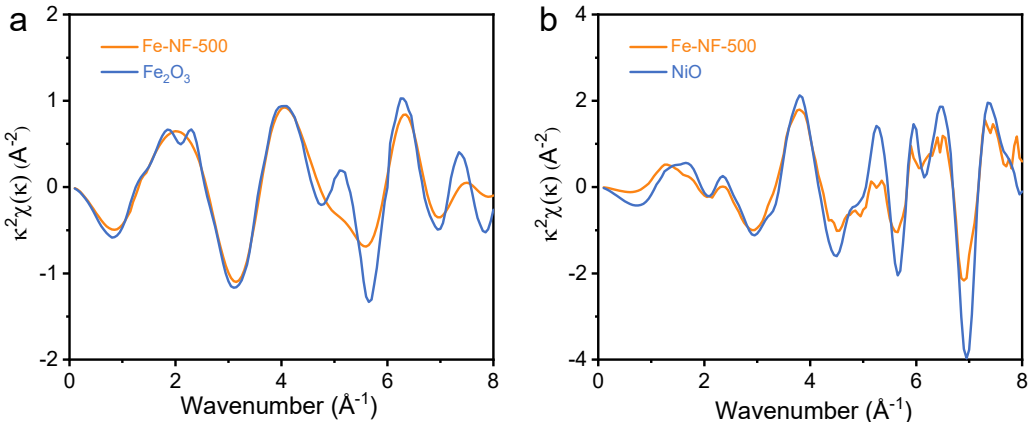

Figure S10. (a) Fe K-edge EXAFS oscillations of Fe_2O_3 and Fe-NF-500. (b) Ni K-edge EXAFS oscillations of NiO and Fe-NF-500.

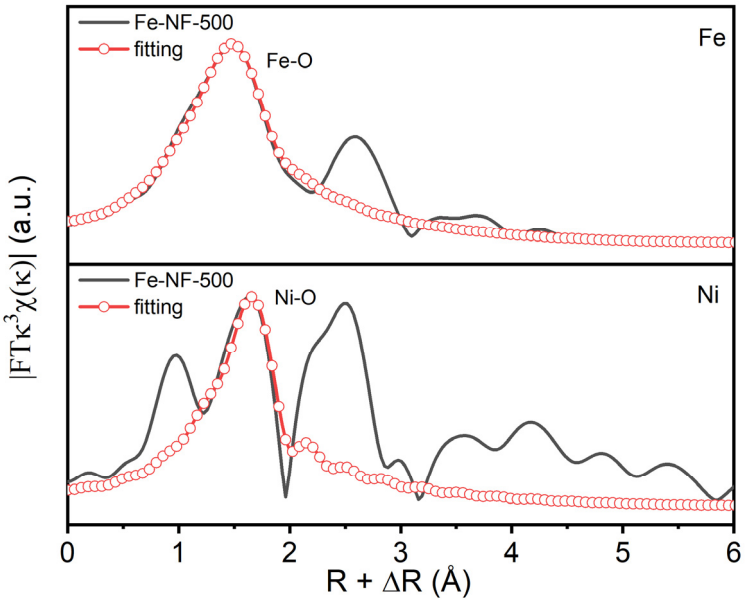

Figure S11. FT-EXAFS spectra of Fe-NF-500.

Table S1. EXAFS fitting parameters of Fe-NF-500. (CNs: coordination numbers; R: bond distance; σ^2: Debye-Waller factors.)

Catalyst	Scattering pair					
	Fe-O			Ni-O		
Fe-NF-500	CNs	R	σ^2	CNs	R	σ^2
	6.0	1.92 (± 0.008)	2.4 (± 0.5)	5.7	2.10 (± 0.01)	4.6 (± 0.7)

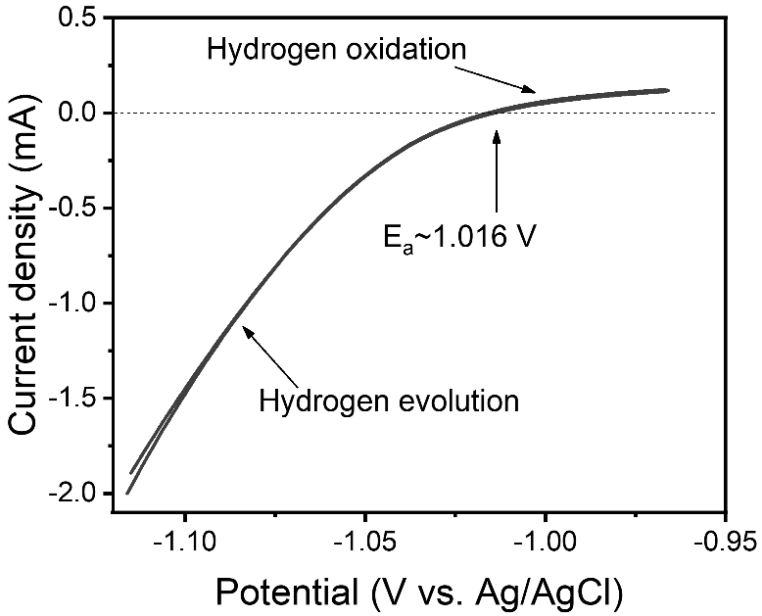

Figure S12. RHE calibration plot. The calibration was performed in the high purity hydrogen saturated electrolyte with a Pt wire as the working electrode. CV were run at a scan rate of 1 mV s^{-1}, and the average of the two potentials at which the current crossed zero was taken to be the thermodynamic potential for the hydrogen electrode reactions.

Table S2. The surface coverage of the NiO/NiOOH redox species in the NiO, NiO/Fe_2O_3 Mixture, and Fe-NF-500.

	NiO	NiO/Fe_2O_3 Mixture	Fe-NF-500
Slope between the cathode peak current density and the scan rates	1.47	1.99	3.89
Surface coverage (Γ*: mol cm^{-2})	1.55×10^{-7}	2.10×10^{-7}	4.14×10^{-7}

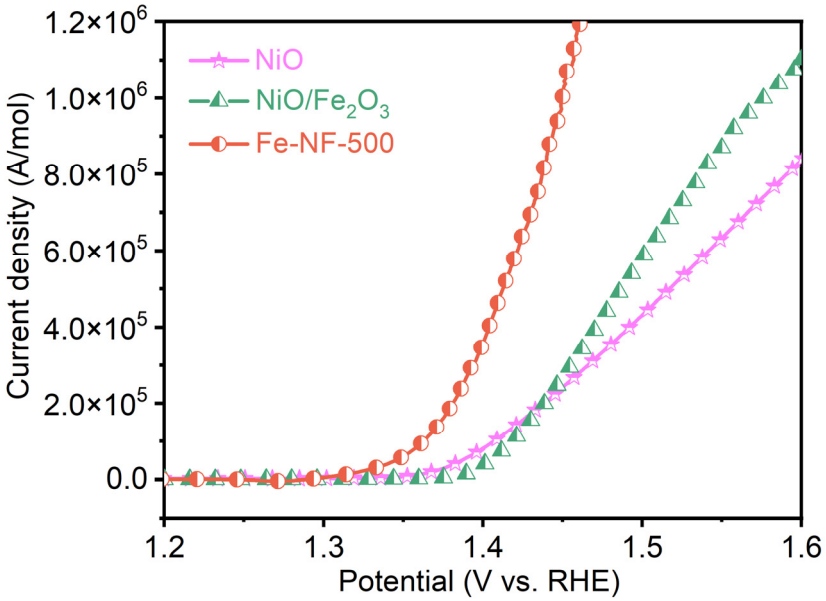

Figure S13. Polarization curves normalized by surface coverage of NiO, NiO/Fe_2O_3, and Fe-NF-500.

Table. S3 The normalized current density of the active site at different potentials.

	j at V=1.43 V ($A\ mol^{-1}_{(\Gamma^*)}$)	j at V=1.45 V ($A\ mol^{-1}_{(\Gamma^*)}$)	j at V=1.47 V ($A\ mol^{-1}_{(\Gamma^*)}$)
NiO	1.601×10^5	2.344×10^5	3.134×10^5
NiO/Fe_2O_3	1.620×10^5	2.709×10^5	3.930×10^5
Fe-NF-500	6.920×10^5	1.002×10^6	1.394×10^6

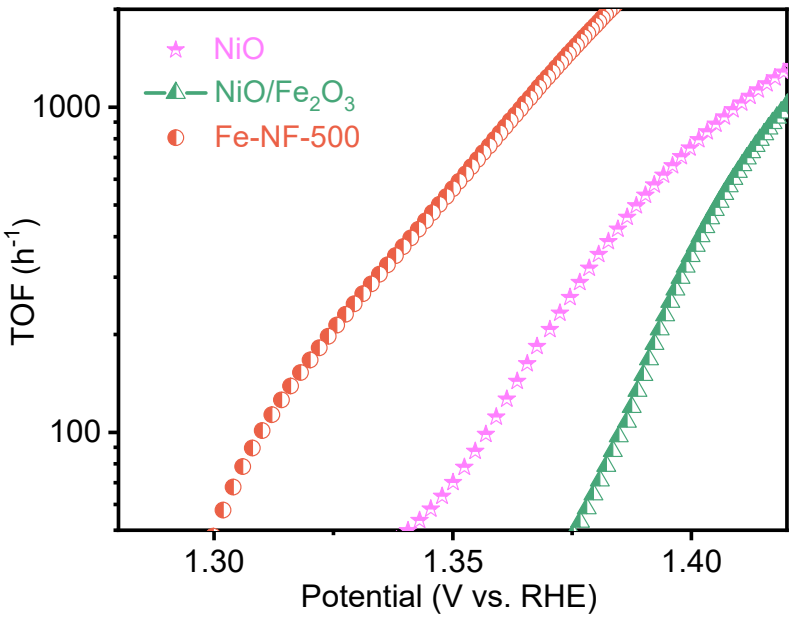

Figure S14. The turnover frequency of the NiO, NiO/Fe_2O_3 and Fe-NF-500 catalysts calculated from polarization curves.

The turnover frequency (TOF) of the catalysts was calculated using following equation:

$$TOF(formate\ h^{-1}) = 3600 \times TOF(formate\ S^{-1}) = 3600 \times \frac{formate\ turnovers\ per\ A_{geo}}{Active\ sites\ per\ A_{geo}}$$

The formate turnover per geometric area was obtained from the geometric current density for the LSV polarization curves according to equation:

$$Formate\ turnover\ per\ A_{geo} = j_{geo} \times \frac{1\ C\ s^{-1}}{1000\ mA} \times \frac{1\ mol}{96485.3\ C} \times \frac{1}{4} \times \frac{6.023 \times 10^{23}}{1\ mol\ Formate}$$

All Ni atoms were assumed to be active sites. Therefore, the number of active sites per geometric area equals the number of Ni atoms per geometric area, which can be calculated from the results of the surface coverage analysis.

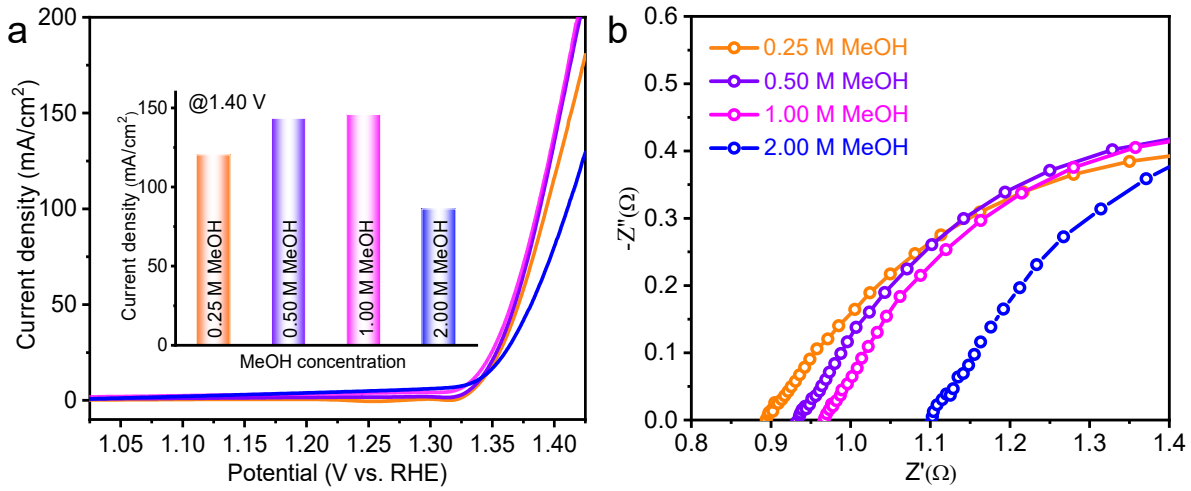

Figure S15. (a) LSV curves of Fe-NF-500 in 1.0 M KOH with different methanol concentration electrolytes and the current density cartogram at 1.4 V in the inset. (b) Nyquist plots of Fe-NF-500 in 1.0 M KOH with different methanol concentration electrolytes.

The MOR current density increased steadily with increasing methanol concentration up to 1.0 M, and the oxidation potential reached only 1.415 V to obtain the current density of 200 mA/cm^2. Nonetheless, a significant decline in oxidation current density was found with a further increasing concentration of methanol. This is ascribed to the change of solution resistance and diffusion coefficient near the electrode hindering further oxidation reaction. Therefore, the concentration of methanol was optimized to 1.0 M.

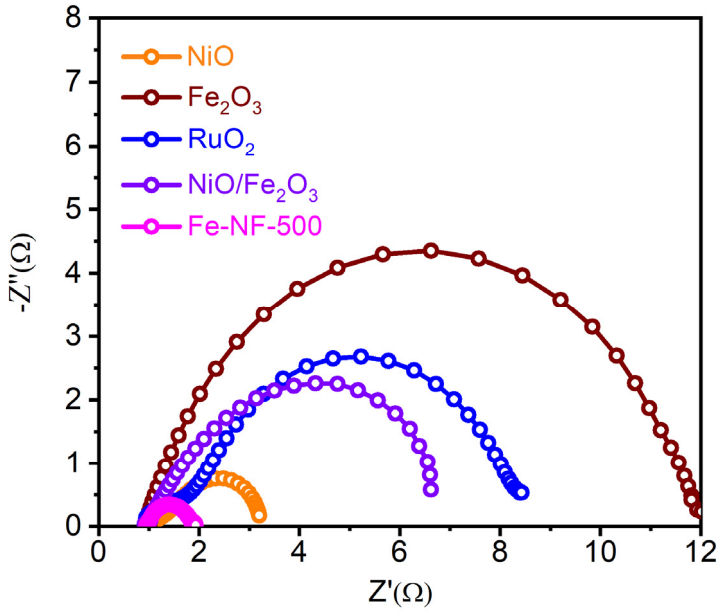

Figure S16. The Nyquist plots over the electrocatalysts in 1.0 M KOH mixed with 1.0 M methanol solution.

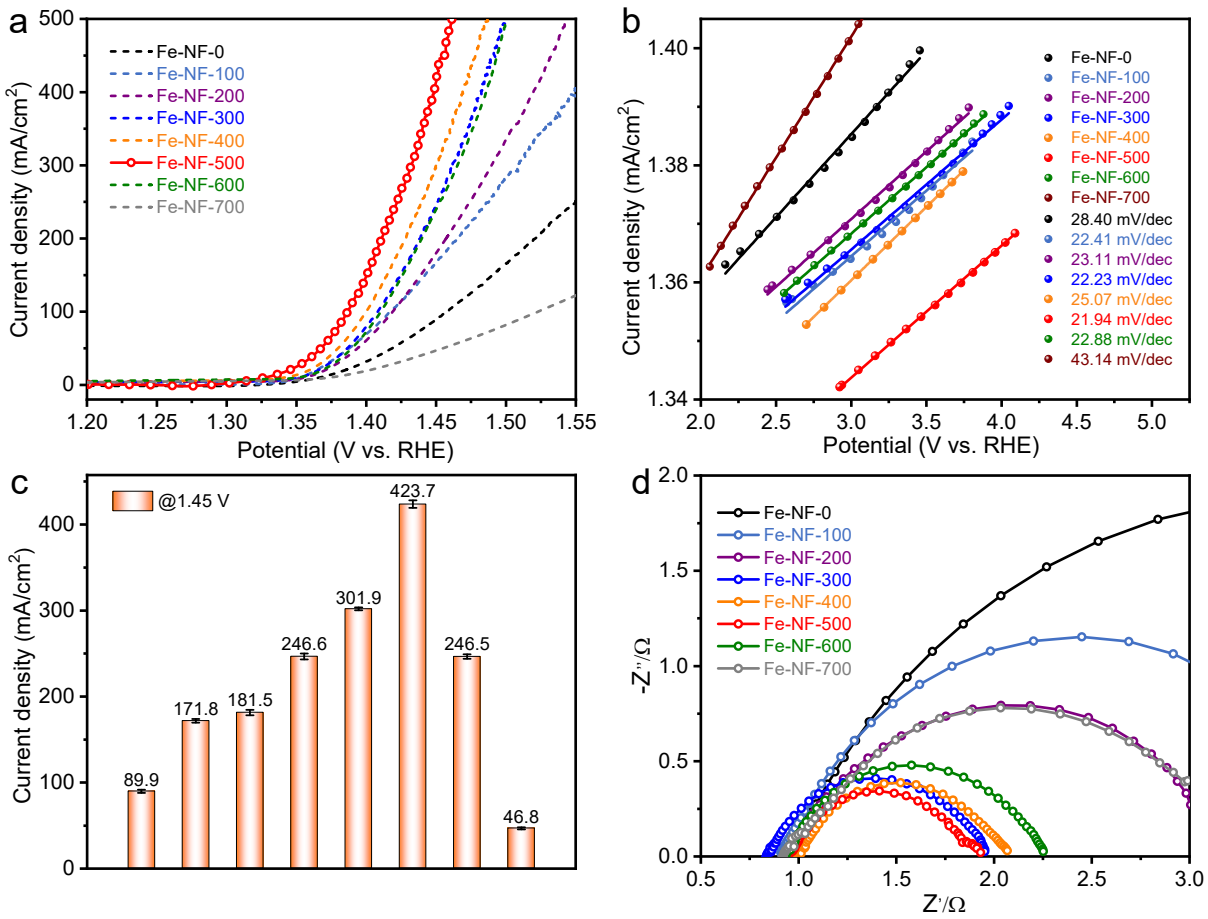

Figure S17. (a) LSV curves of Fe -NF-X heterojunctions in 1.0 M KOH solution in the presence of 1.0 M methanol at a scan rate of 50 mV s^{-1}. (b) The specific activities of Fe -NF-X heterojunctions normalized with a geometric area at 1.45 V vs. RHE. (c) Tafel slope and (d) EIS spectra of various electrocatalysts.

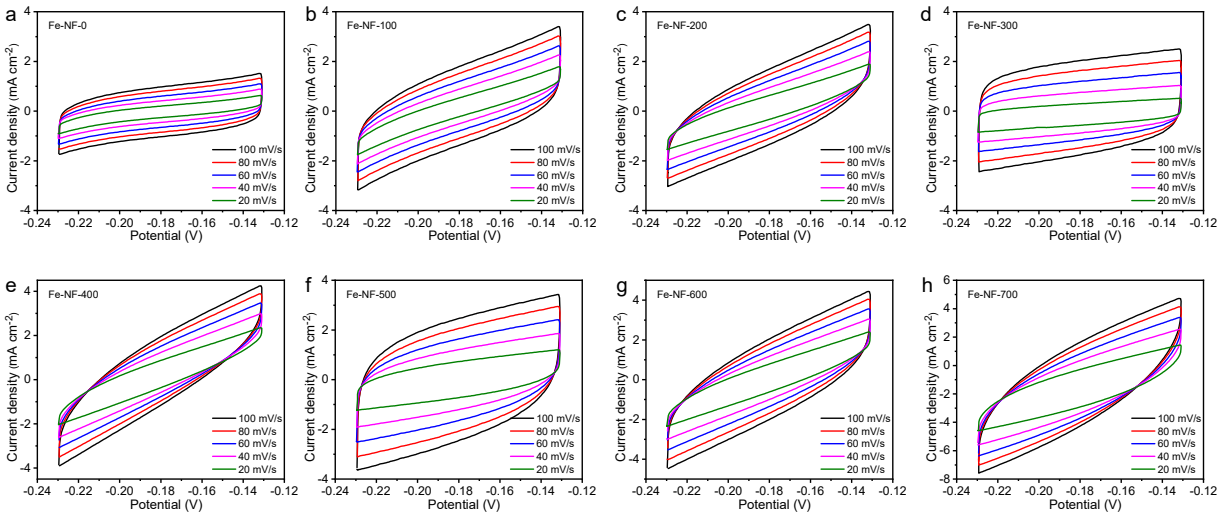

Figure S18. (a-h) Double layer capacitance measurements for determining electrochemical surface areas. Cyclic voltammograms recoded at different scanning rates.

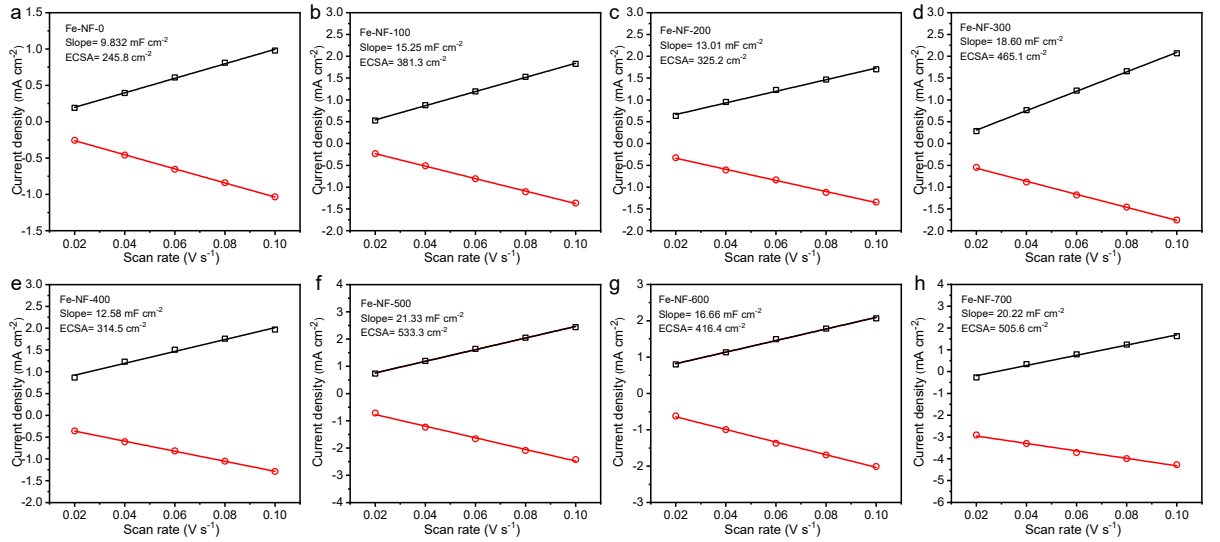

Figure S19. (a-h) The cathodic (red cycle) and the anodic (black square) charging currents measured at 1.1 V vs. RHE plotted as a function of the scanning rates for various electrocatalysts.

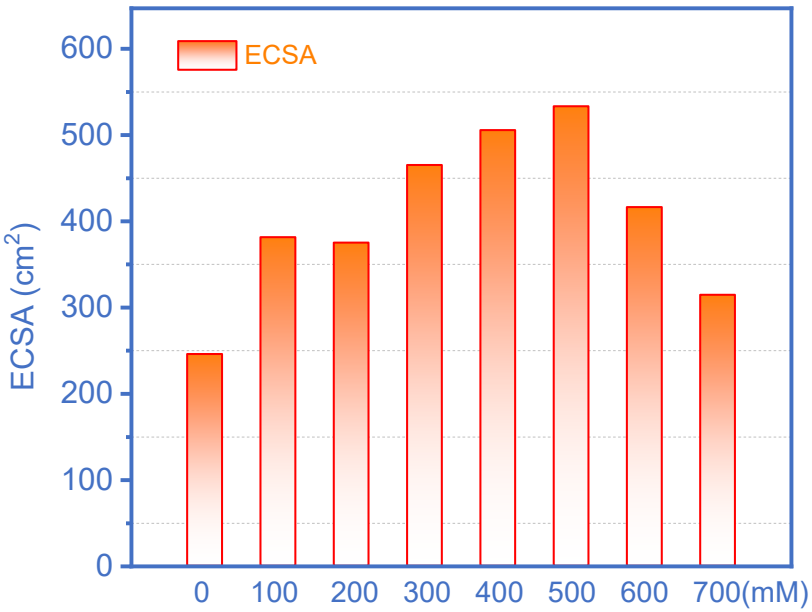

Figure S20. The calculated electrochemical surface area (ECSA) of Fe-NF-0, Fe-NF-100, Fe-NF-200, Fe-NF-300, Fe-NF-400, Fe-NF-500, Fe-NF-600, and Fe-NF-700.

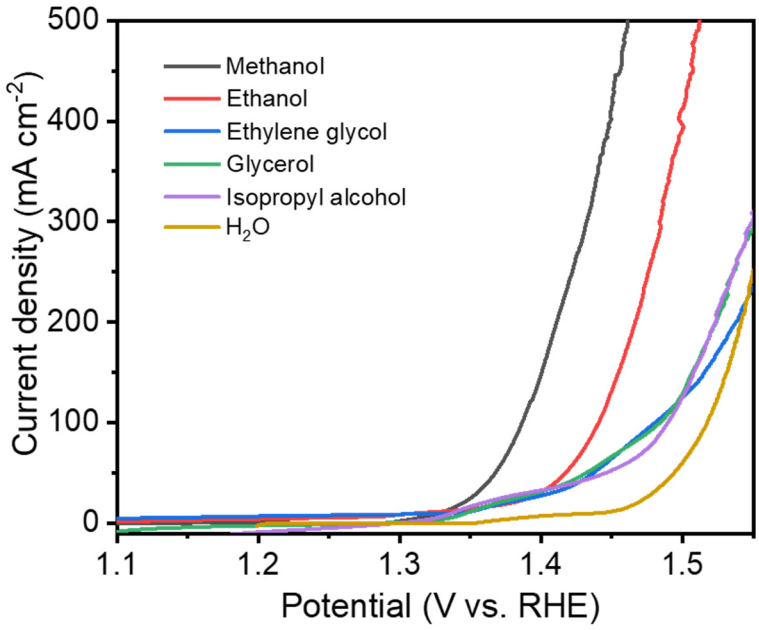

Figure S21. LSV curves of Fe-NF-500 heterojunction in 1.0 M KOH + 1.0 M methanol, 1.0 M KOH + 1.0 M ethanol, 1.0 M KOH + 1.0 M ethylene glycol, 1.0 M KOH + 1.0 M glycerol, 1.0 M KOH + 1.0 M isopropyl alcohol, and 1.0 M KOH, respectively.

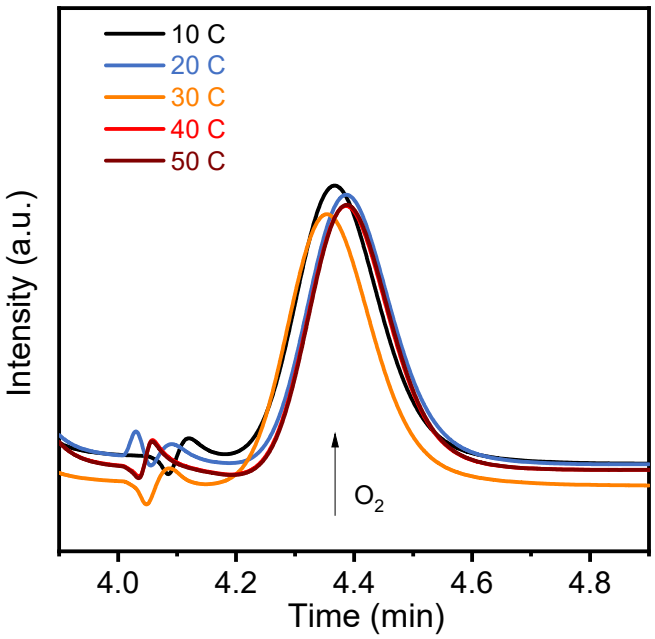

Figure S22. Chromatographic curves of O_2 measured by IC as a function of charges on anode under cell voltage of 1.50 V for Fe-NF-500.

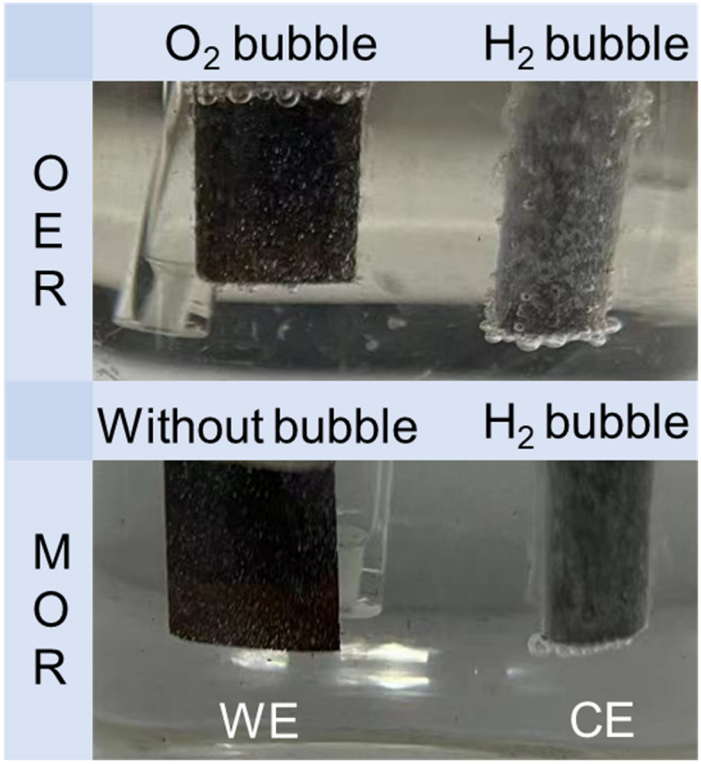

Figure S23. Electronic photographs of the electrodes in the MOR and OER. Visible O_2 bubbles release is accompanied by further OER forward scanning. However, the bubbles are not seen in a water-alcohol mixed electrolyte at the Fe-NF-500 anode.

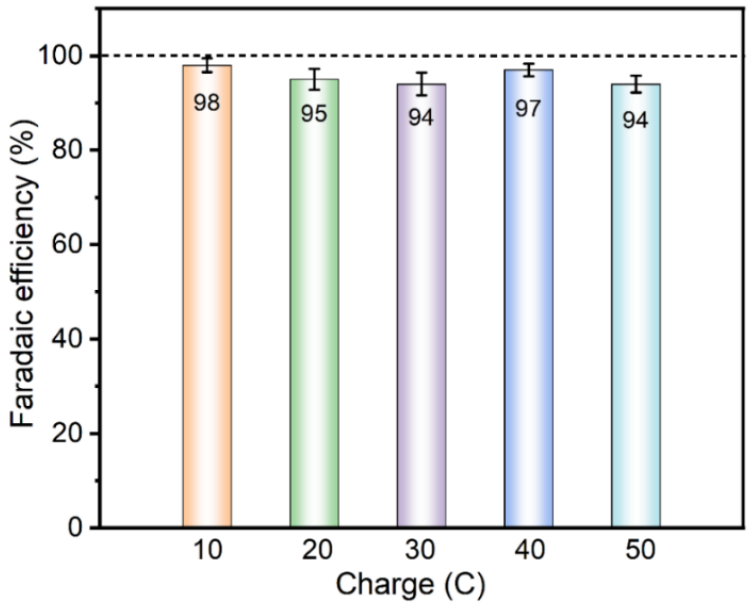

Figure S24. The calculated Faradaic efficiencies of formate at anode.

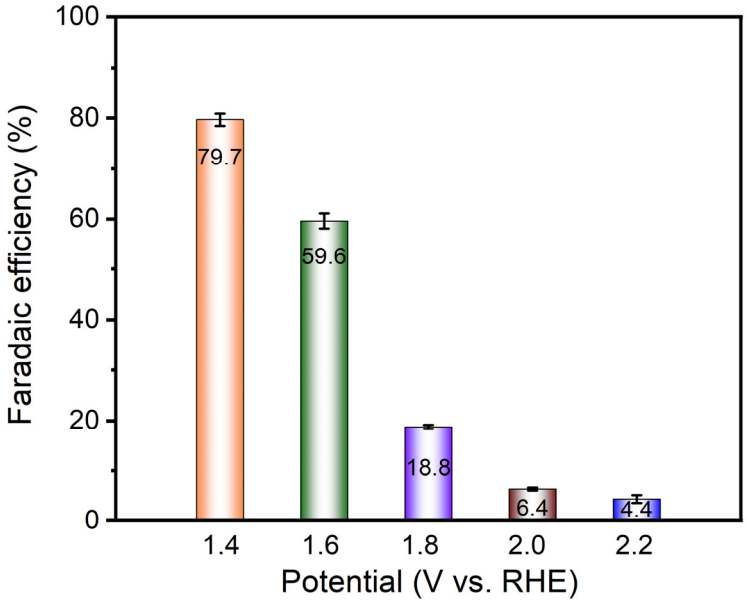

Figure S25. The calculated voltage-dependent Faradaic efficiencies of formate generation.

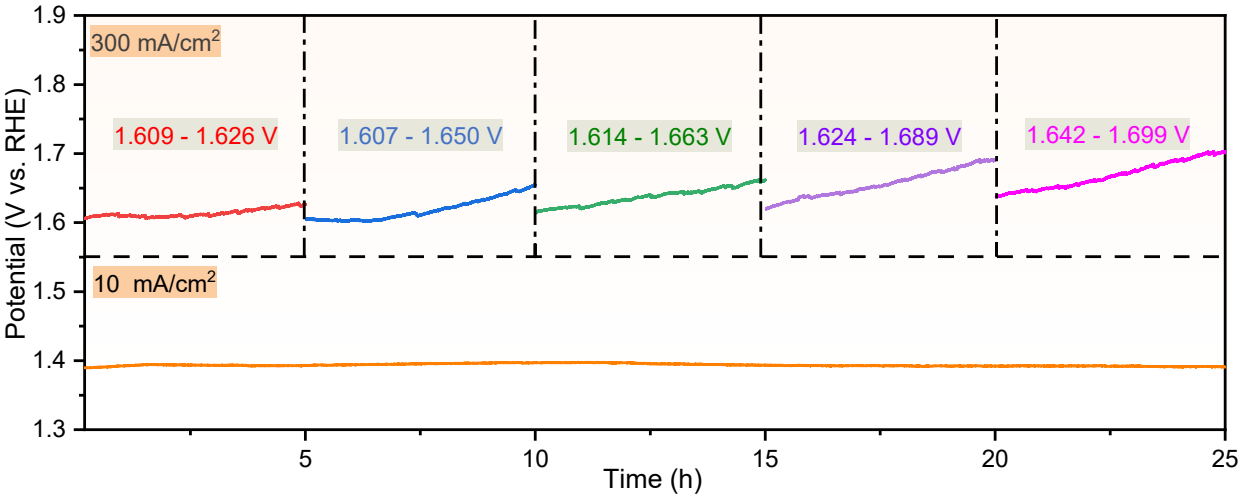

Figure S26. The chronopotentiometry curves of methanol upgrading reaction at a corrected current density of 10 mA cm^{-2} and 300 mA cm^{-2}.

This two-electrode membrane-free system also displayed significant durability that can be observed during 25 h electrolysis at a current density of 10 and 300 mA cm^{-2}. In particular, after 5 cycles of reaction, the driving potential decreased by only 30 mV after 5 cycles.

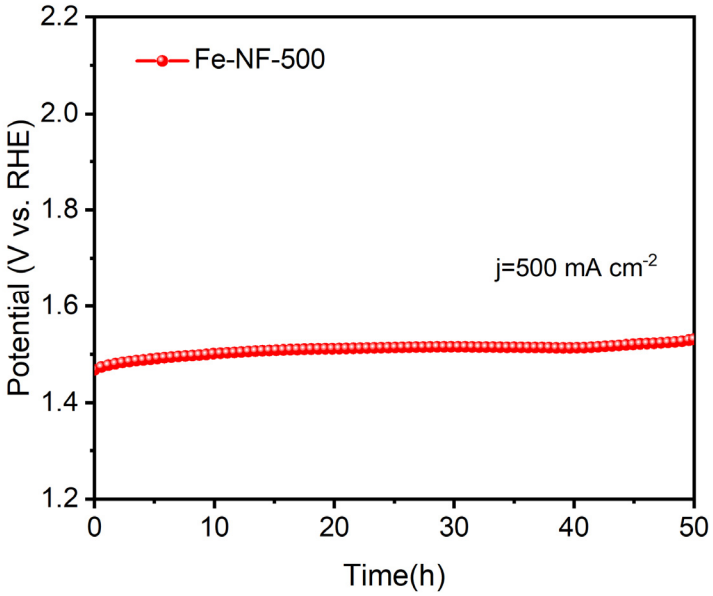

Figure S27. The chronopotentiometry curves of methanol upgrading reaction at a corrected current density of 10 mA cm^{-2}.

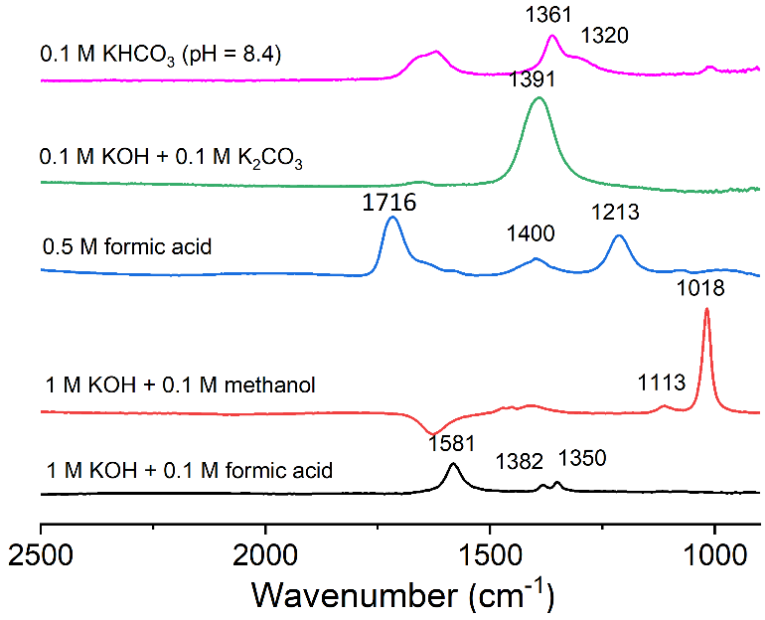

Figure S28. Standard spectra of various possible species in methanol oxidation reaction in alkaline media. Data were recorded by the ATR mode on a ZnSe prism.

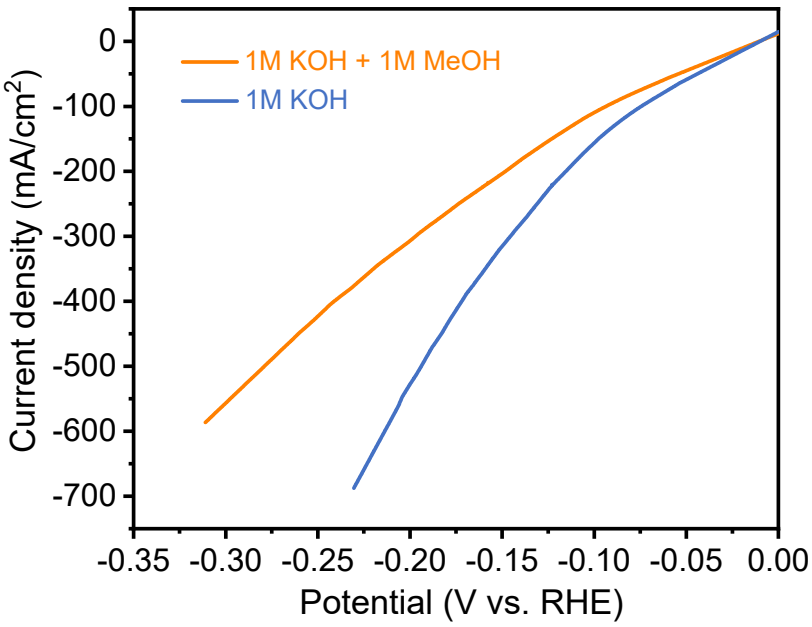

Figure S29. LSV curves of $MoNi_4$ for the HER in 1.0 M KOH and 1.0 M KOH + 1.0 M methanol solution with a scan rate of 5 mV s^{-1}.

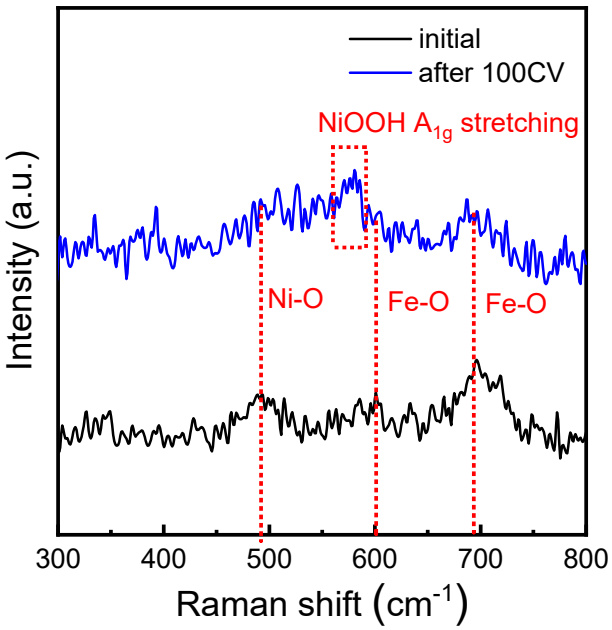

Figure S30. Raman spectra of Fe-NF-500 before and after the cycling reaction. A typical phonon vibration peak of nickel oxide is located at 490 cm^{-1}, [Nanoscale Research Lett. 2011, 6, 485] and the Fe_2O_3 peak located at 601 and 693 cm^{-1} did not change after CV cycles. The appearance of a new Raman peak at 576 cm^{-1}, which can be attributed to the surface hydroxylation of nickel oxide.

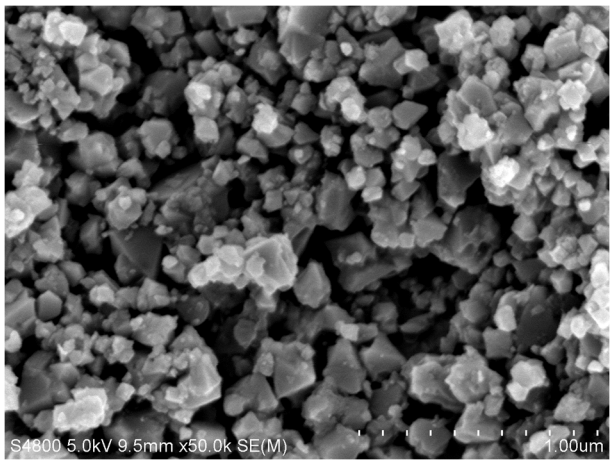

Figure S31. SEM images of Fe-NF-500 after cycling reaction.

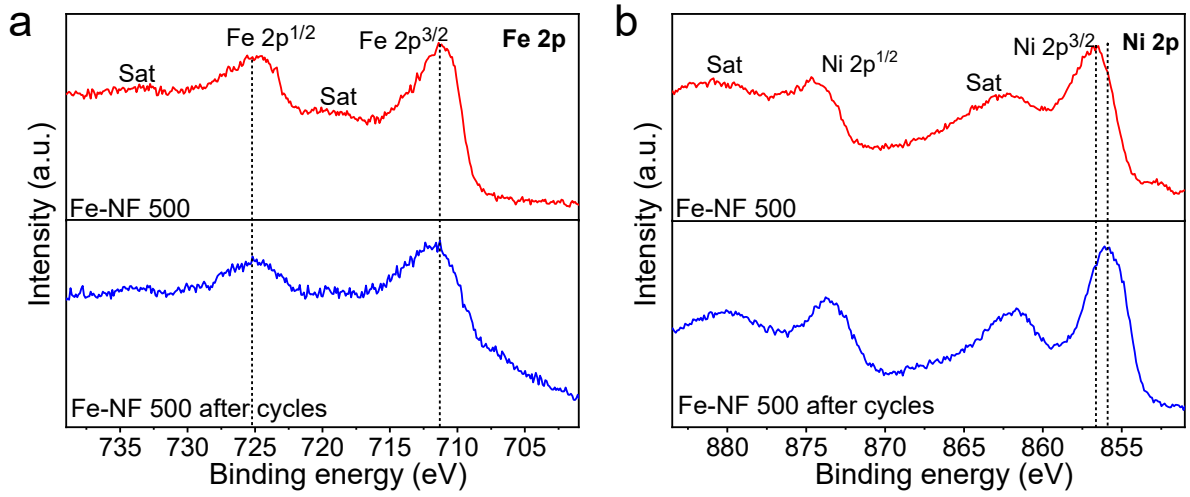

Figure S32. XPS spectra before and after the cycling reaction of (a) Fe and (b) Ni.

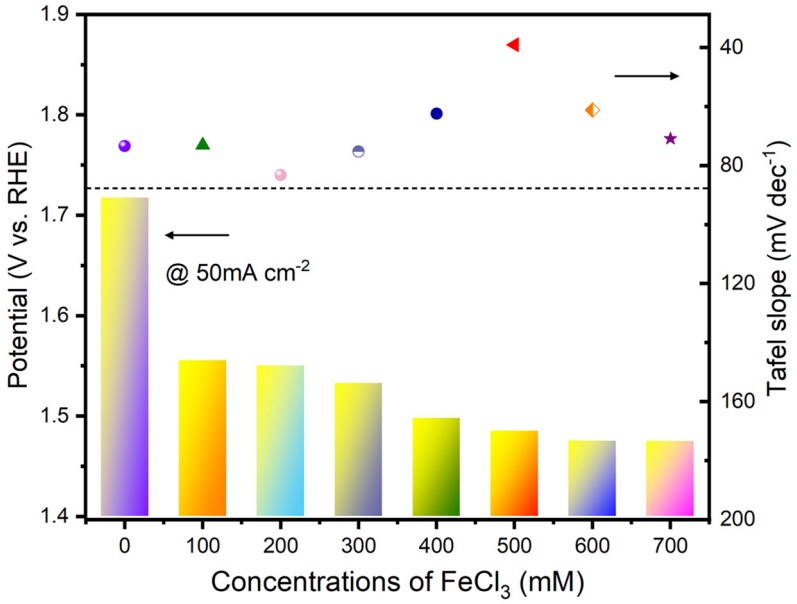

Figure S33. Overpotential and tafel slope of Fe_2O_3/NiO-NF heterojunctions in 1.0 M KOH solution at a scan rate of 50 mV s^{-1}.

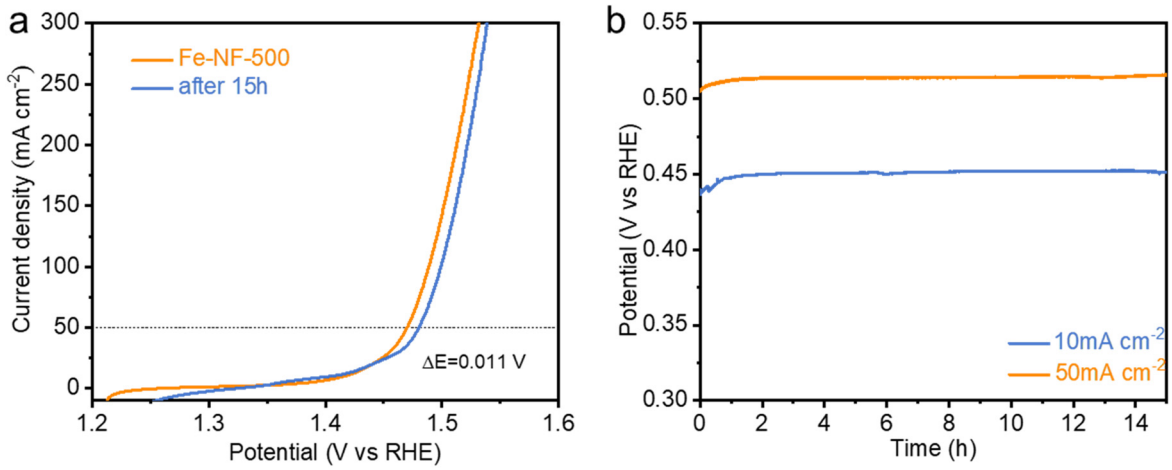

Figure S34. (a) Continuous cycling CV curves in the potential range 1.2-1.6 V with a scan rate of 100 mV s^{-1}. (b) The long-term continuous water electrolysis at a current density of 10 mA cm^{-2} and 50 mA cm^{-2}.

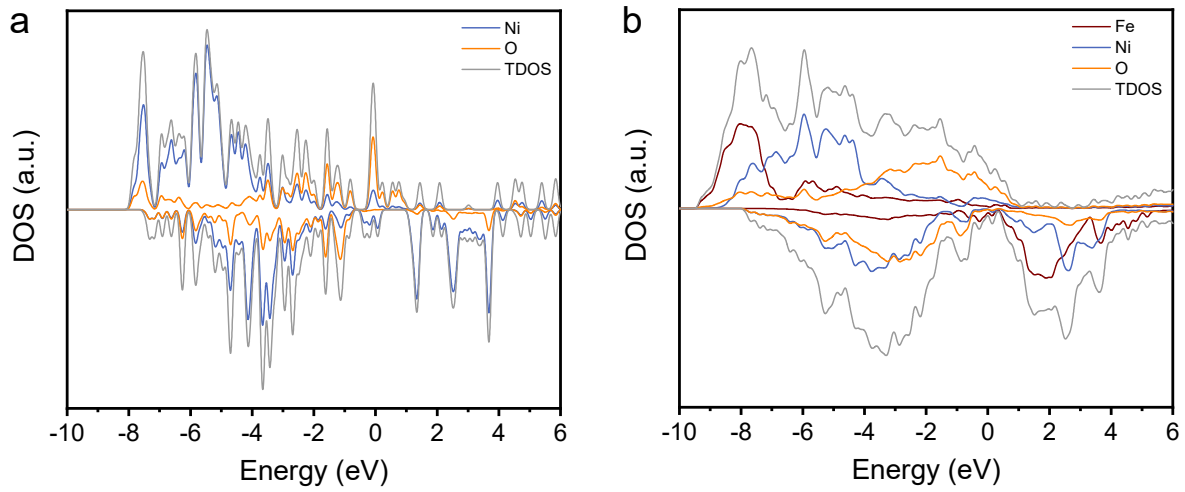

Figure S35. Density of states of NiO and Fe_2O_3/NiO, respectively.

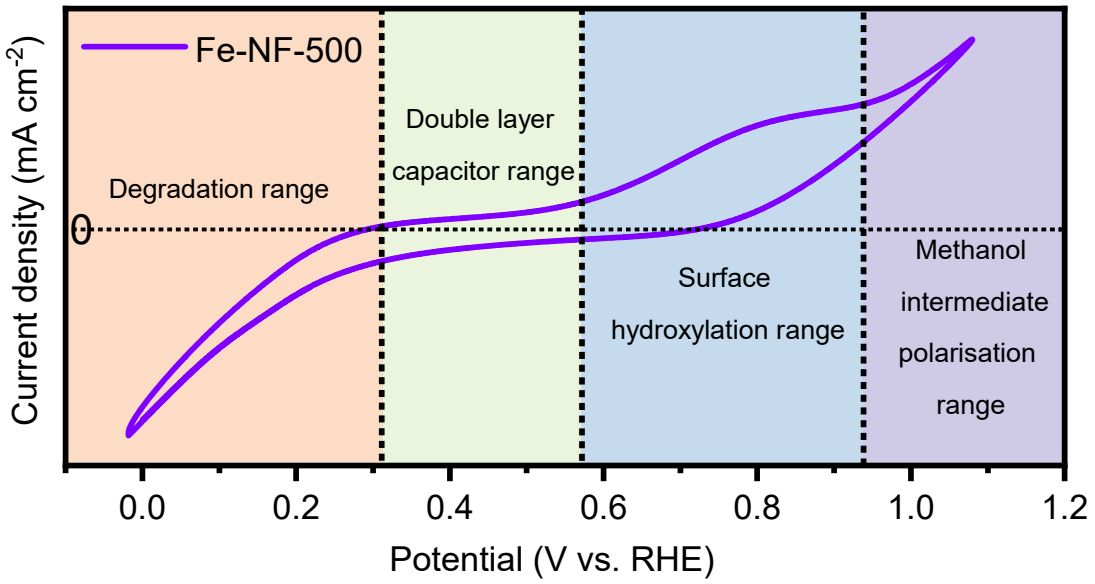

Figure S36. Cyclic voltammogram of Fe-NF-500 in 1.0 M KOH solution with 1.0 M methanol.

To investigate the hydroxylation/de-hydroxylation on the catalyst's surface, electrochemical experiment correlated with proton transfer was conducted. We examined the cyclic voltammetric curve of Fe-NF-500 (Figure. S36) at a range of 0 - 1.1 V vs. RHE. The CV includs a pair of redox peaks at 0.80 V and 0.73 V (vs. RHE), which are often attributed to surface redox transitions of hydroxylation and de-hydroxylation. So, hydroxylation of nickel oxide surfaces is identified as the first step in the MOR mechanism. Furthermore, in the process of polarization only oxidation behavior is present which is manifested in the phase change between NiO and NiOOH (Figure S30). This also confirms that hydroxylation of the nickel oxide surface is the first step in the MOR mechanism.

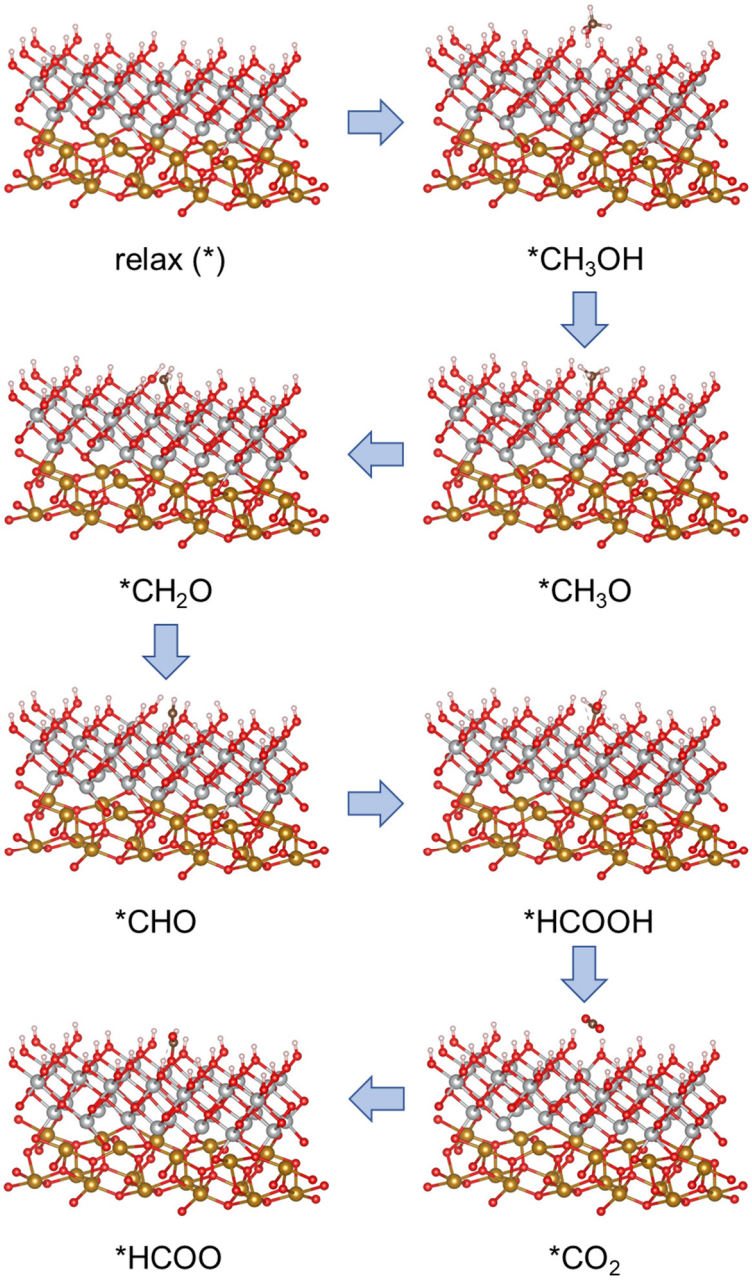

Figure S37. DFT optimized structures of the adsorbed intermediates on the Ni sites in interface models. The red, silver and yellow spheres represent oxygen, nickel and iron atoms respectively.

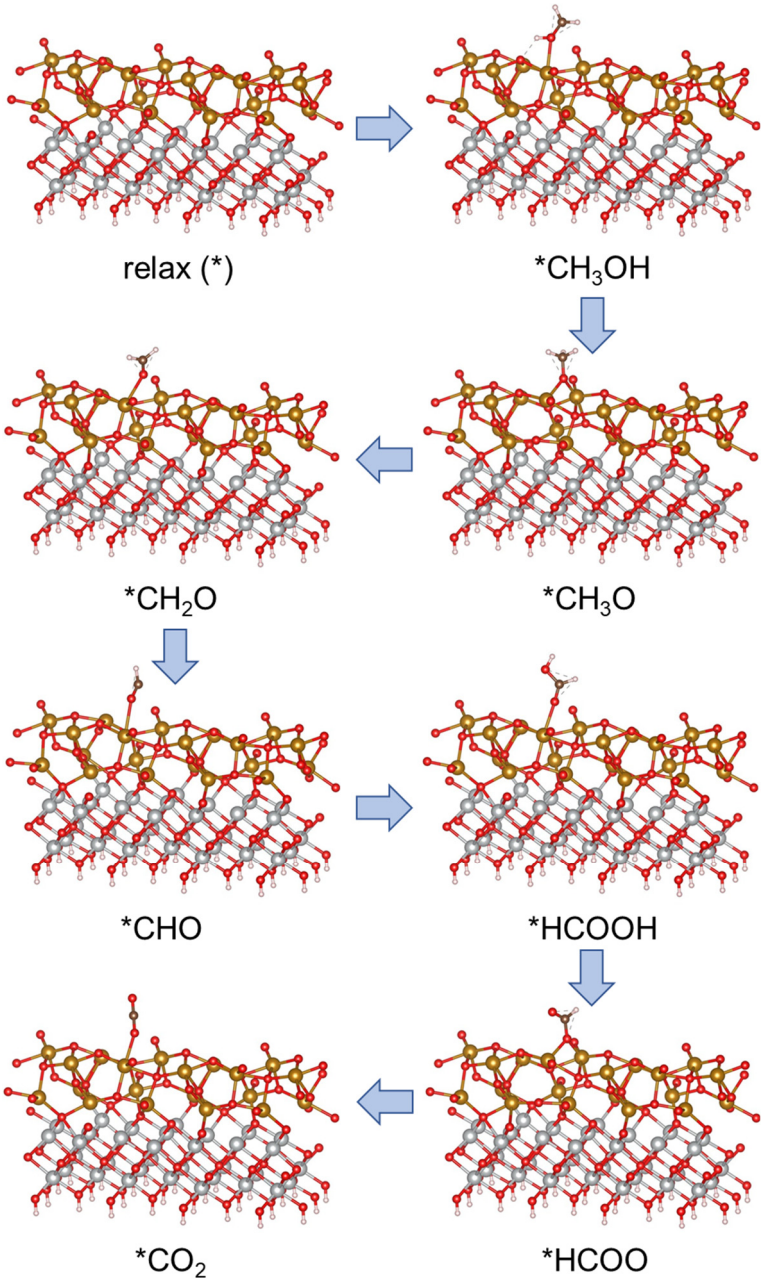

Figure S38. DFT optimized structures of the adsorbed intermediates on the Fe sites in interface models. The red, silver and yellow spheres represent oxygen, nickel and iron atoms respectively.

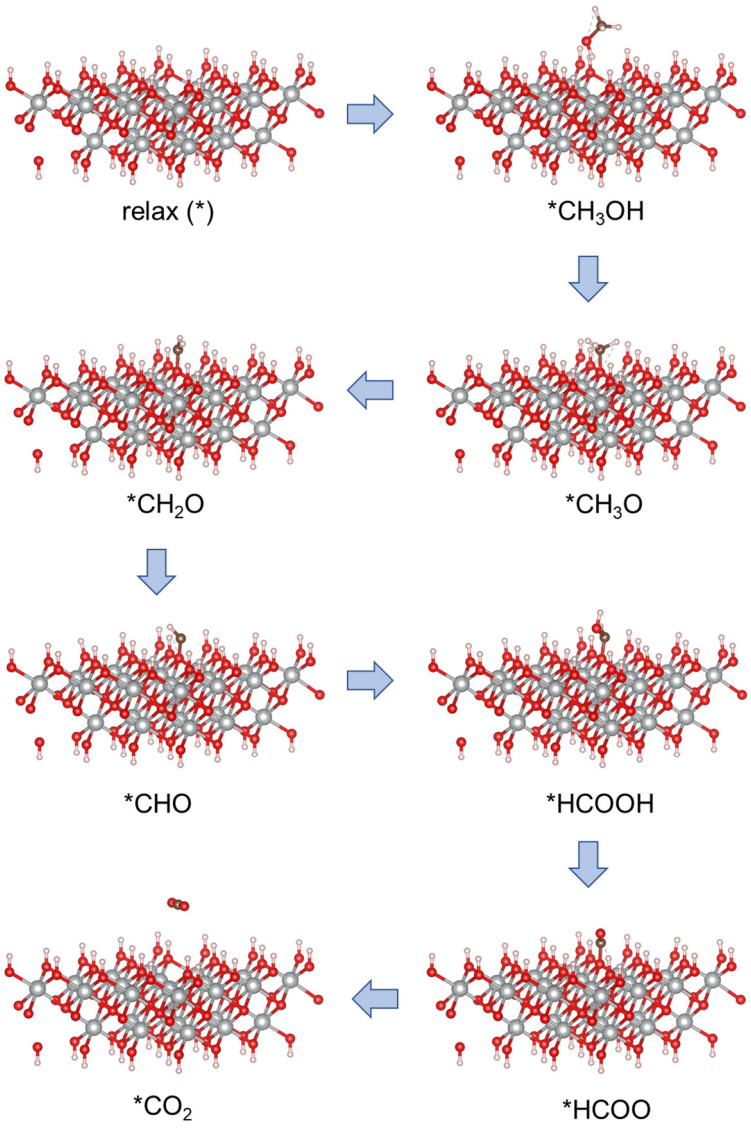

Figure S39. DFT optimized structures of the adsorbed intermediates on the NiO (111) surface. The red, silver and yellow spheres represent oxygen, nickel and iron atoms respectively.

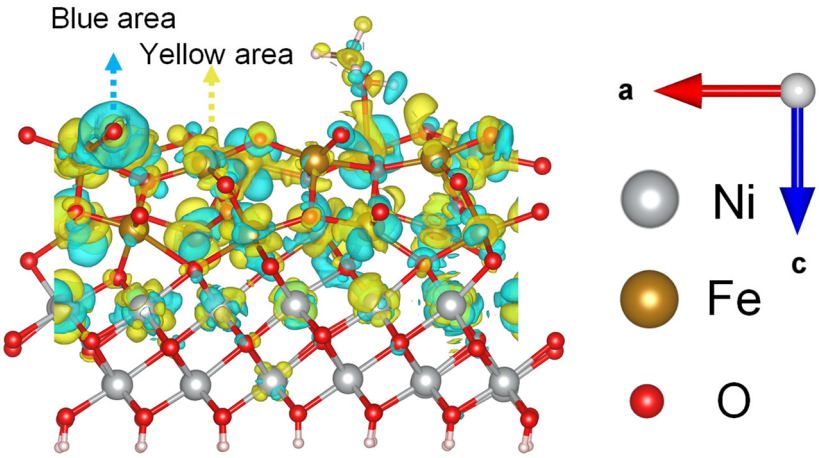

Figure S40. Differential charge density diagram of the interaction between the methanol molecule and the O on the Fe_2O_3 surface. (The blue area represents a decrease in electron density and the yellow area represents an increase in electron density.)

Table S4. Comparison of the anodic organic upgrading reaction performance on non-noble electrocatalysts.

Electrocatalyst	Performance	Electrolyte	Ref.
Fe-NF-500	**10 mA cm^{-2}/1.33 V vs. RHE 100 mA cm^{-2}/1.39 V vs. RHE 576 mA cm^{-2} /1.47 V vs. RHE**	**1.0 M KOH + 1.0 M CH_3OH**	**This work**
$CoNi_{0.25}P$	500 mA cm^{-2} /1.8 V vs. RHE	PET hydrolysate	Nat. Commun. 2021, 12:4679.
NiB-400	500 mA cm^{-2} /1.54 V vs. RHE	1.0 M KOH + 1.0 M CH_3OH	Nat. Commun. 2022 13:4602
Ni-NF-Af	10 mA cm^{-2}/1.345 V vs. RHE	1.0 M KOH + 0.5 M CH_3OH	Adv. Mater. 2021, 33, 2008631.
MnO_2 /CP	10 mA cm^{-2}/1.36 V vs. RHE 90 mA cm^{-2}/1.70 V vs. RHE	0.005 M H_2SO_4 + 0.2 M glycerol	Angew. Chem. Int. Ed. 2021, 60, 21464-21472.
Ni-WO_x	100 mA cm^{-2}/1.40 V vs. RHE	1.0 M KOH + 0.33 M Urea	Angew. Chem. Int. Ed. 2021, 60, 10577 -10582.
Ni_xBi_y aerogels	10 mA cm^{-2}/1.34 V vs. RHE 199 mA cm^{-2}/1.65 V vs. RHE	1.0 M KOH + 1.0 M CH_3OH	Angew. Chem. Int. Ed. 2020, 59, 13891-13899.
Ni_3C	84 mA cm^{-2}/1.60 V vs. RHE	1.0 M KOH + 1.0 M CH_3OH	Angew. Chem. Int. Ed. 2020, 59, 20826-20830.
$Ni_{0.75}Cu_{0.25}$	10 mA cm^{-2}/1.40 V vs. RHE 160 mA cm^{-2}/1.78 V vs. RHE	1.0 M KOH + 1.0 M CH_3OH	Angew. Chem. Int. Ed. 2017, 129, 4559-4564.
A-Ni-Co-H/NF	400 mA cm^{-2} /1.45 V vs. RHE	1.0 M KOH + 0.1 M benzyl alcohol	Energy Environ. Sci. 2020, 13, 4990-4999.
RhSA-S-Co_3O_4	10 mA cm^{-2} /1.28 V vs. RHE 300 mA cm^{-2} /1.48 V vs. RHE	1.0 M KOH + 0.5 M urea	Energy Environ. Sci. 2021, 14, 6494-6505.
NiO@C/CC	119.1 mA cm^{-2}/1.67 V vs. RHE	1.0 M KOH + 1.0 M CH_3OH	Adv. Energy Mater. 2020, 10, 2001397.
$Co(OH)_2$@HOS/CP	100 mA cm^{-2}/1.53 V vs RHE	1.0 M KOH + 1.0 M CH_3OH	Adv. Funct. Mater. 2020, 30, 1909610.
h-NiSe/ CNTs/CC	400 mA cm^{-2}/1.65 V vs RHE	1.0 M KOH + 1.0 M CH_3OH	Adv. Funct. Mater. 2021, 31, 2008812.
NiMoP	100 mA cm^{-2}/1.41 V vs RHE	1.0 M KOH + 0.5 M Urea	Adv. Funct. Mater. 2021, 2104951.
Fe-Ni NPs	10 mA cm^{-2}/1.40 V vs. RHE	1.0 M KOH + 1.0 M CH_3OH	ACS Catal. 2017, 7, 365-379.
$Ni(OH)_2$ nanosheet arrays	100 mA cm^{-2}/1.36 V vs. RHE	1.0 M KOH + 1.0 M CH_3OH	Appl. Catal. B: Environ. 2021, 281, 119510.
$NiCoMnO_4$/N-rGO	10 mA cm^{-2}/1.50 V vs. RHE	1.0 M KOH + 1.0 M CH_3OH	Appl. Catal. B: Environ. 2017, 201, 241-252.
VO-rich ultrathin NiO	85.3 mA cm^{-2}/1.70 V vs. RHE	1.0 M KOH + 1.0 M CH_3OH	Appl. Catal. B: Environ. 2019, 244, 1096-1102.
Cu-Ni/CN	45 mA cm^{-2}/1.60 V vs. RHE	1.0 M KOH + 1.0 M CH_3OH	Appl. Catal. B: Environ. 2019, 244, 272-283.
NiSn bimetallic nanoparticles	10 mA cm^{-2}/1.43 V vs. RHE 120 mA cm^{-2}/1.98 V vs. RHE	1.0 M KOH + 1.0 M CH_3OH	Appl. Catal. B: Environ. 2018, 234, 10-18.

$Ni_2Fe(CN)_6$	100 mA cm^{-2}/1.35 V vs. RHE	1.0 M KOH + 0.33 M Urea	Nat. Energy 2021, 904-912.
hollow Mn doped $Ni(OH)_2$	16.4 $mAmg^{-1}$/1.55 V vs. RHE	1.0 M KOH + 1.0 M CH_3OH	Nano Energy 2019, 55, 37-41.
Ni_3S_2-CNFs	> 700 mA cm^{-2}/2.02 V vs. RHE	1.0 M KOH + 1.0 M CH_3OH	Nano Energy 2021, 80,105530.
$Cu(OH)_2@CoCO_3(OH)_2$	223 mA cm^{-2}/0.50 V vs. SCE	1.0 M KOH + 0.5 M CH_3OH	Small 2017, 13, 1602755.
$Ni_{0.75}Fe_{0.25}Se_2$	160 mA cm^{-2}/1.68 V vs. RHE	1.0 M KOH + 0.5 M CH_3OH	Small 2021, 17, 2006623.
Co_2P@Co/N-C	7 mA cm^{-2}/0.60 V vs. SCE	1.0 M KOH + 0.5 M CH_3OH	Small 2017, 13, 1700796.
Mo modified Co_4N	10 mA cm^{-2}/1.36V vs. RHE 100 mA cm^{-2}/1.48V vs. RHE	1.0 M KOH + 1.0 M CH_3OH	J. Mater. Chem. A 2021, 9, 21094-21100.
CNFs@NiSe	10 mA cm^{-2}/1.38V vs. RHE 100 mA cm^{-2}/1.51V vs. RHE	1.0 M KOH + 1.0 M CH_3OH	J. Mater. Chem. A 2019, 7, 25878-25886.
CZIF-CoCu	551 A g^{-1}/0.695 V vs. SCE.	1.0 M KOH + 1.0 M CH_3OH	J. Mater. Chem. A 2020, 8, 12285-12290.
$Ni(OH)_2$/NF	400 mA cm^{-2}/1.53V vs. RHE	1.0 M KOH + 0.5 M CH_3OH	Chem. Eng. J. 412, 2021, 127893.